Spatial distribution of the plasma parameters in the RF negative ion source prototype for fusion

S. Lishev' , L. Schiesko, D. Wünderlich, and U. Fantz

Citation: AIP Conference Proceedings **1655**, 040010 (2015); doi: 10.1063/1.4916452
View online: http://dx.doi.org/10.1063/1.4916452
View Table of Contents: http://aip.scitation.org/toc/apc/1655/1
Published by the American Institute of Physics

Spatial Distribution of the Plasma Parameters in the RF Negative Ion Source Prototype for Fusion

S. Lishev[1, a)], L. Schiesko[2], D. Wünderlich[2] and U. Fantz[2]

[1]*Faculty of Physics, Sofia University, BG-1164 Sofia, Bulgaria*
[2]*Max-Planck-Institut für Plasmaphysik, 85748 Garching, Germany*

[a)]lishev@phys.uni-sofia.bg

Abstract. A numerical model, based on the fluid plasma theory, has been used for description of the spatial distribution of the plasma parameters (electron density and temperature, plasma potential as well as densities of the three types of positive hydrogen ions) in the IPP prototype RF negative hydrogen ion source. The model covers the driver and the expansion plasma region of the source with their actual size and accounts for the presence of the magnetic filter field with its actual value and location as well as for the bias potential applied to the plasma grid. The obtained results show that without a magnetic filter the two 2D geometries considered, respectively, with an axial symmetry and a planar one, represent accurately the complex 3D structure of the source. The 2D model with a planar symmetry (where the E×B and diamagnetic drifts could be involved in the description) has been used for analysis of the influence, via the charged-particle and electron-energy fluxes, of the magnetic filter and of the bias potential on the spatial structure of the plasma parameters in the source. Benchmarking of results from the code to experimental data shows that the model reproduces the general trend in the axial behavior of the plasma parameters in the source.

INTRODUCTION

Magnetized plasma sources have a wide range of different applications not only in the industry [1] and as dc particle sources for accelerators, but also to the neutral beam injection (NBI) systems for fusion [2]. The IPP prototype RF caesiated negative-hydrogen-ion source is chosen as the reference design for the ITER NBI system [3]. At short pulse operation (4 s) and low gas-pressure (0.3 Pa), the source fulfills the ITER requirements by achieving an accelerated negative hydrogen-ion-beam current of 330 A/m^2, with a ratio of the co-extracted electrons less than one [4-6]. The source is an RF inductively driven tandem type source based on surface production of the ions with a cylindrical driver, a bigger volume expansion chamber and magnetic filter (MF) [4]. The latter is formed by permanent magnets located on the external sides of the expansion region and can be moved from the plasma grid (PG) to the driver exit. The filter fields are such that, among the charged particles, only the electrons are magnetized. The magnetic filter plays a key role in the overall operation of the source, since it reduces the rate of negative ions destruction (by means of collisions) in the source plasma and simultaneously the current of the co-extracted electrons. However, the MF has a strong impact on the homogeneity of the plasma parameters in the expansion plasma volume [7]. This issue forces studies on the spatial distribution of the plasma parameters in the source. Due to the limited accessibility for diagnostics in the large-size and high-power sources, an achievement of a complete picture of the spatial structure of the plasma parameters is only possible by modeling the source plasma.

Previously applied models (fluid [8, 9] and PIC [10] models) showed that transport processes are in the basis of the electron cooling and of the spatial distribution of the electron density. Moreover, due to the E×B and diamagnetic drifts, as well as to the electron energy fluxes related to them, the spatial symmetry of the plasma parameters is broken. In addition, the RF power deposition localized in the driver of the sources and the operation at a low gas pressure introduce a plasma expansion region that brings a strong nonlocality in the discharge behavior, via effects of charged particles and energy fluxes [11]. In this source, the injection of (40 – 80) kW at a low gas

Fourth International Symposium on Negative Ions, Beams and Sources (NIBS 2014)
AIP Conf. Proc. 1655, 040010-1–040010-10; doi: 10.1063/1.4916452

pressure, combined with the presence of a magnetic field in the expansion region makes it necessary to model the source in its globality.

Usually these models involve assumptions and simplifications that have their physical background, but with regards to their applicability to a given source, a benchmark with experiments or, at least, with other codes is required. The specific geometry of the IPP prototype RF source (cylindrical driver and rectangular expansion plasma volume) in combination with the three-dimensional topology of the magnetic filter field, calls for a 3D model description. However, this is a complex and time-consuming task, and the problem is, usually, treated as a 2D one [8-10].

This work aims at providing numerical results for the spatial structure of the plasma parameters in the IPP prototype RF negative-hydrogen-ion source. A previous model of the interaction of a plasma with a transverse MF [8], developed within the fluid plasma approach, has been used. It is extended to the configuration and operational conditions of the IPP prototype RF source, accounting for the magnetic filter field with its actual value and location as well as for the plasma grid with the bias potential applied to it. The study stresses on three aspects: (i) choice of a proper geometry in the model, (ii) influence, via the charged-particle and electron-energy fluxes, of the magnetic filter and of the bias potential applied to the plasma grid on the spatial structure of the discharge, and (iii) benchmarking of the code to experimental results.

FORMULATION OF THE PROBLEM AND SET OF EQUATIONS

The main difficulties in modeling the IPP RF prototype source are caused by: (i) the geometry of the source (a cylindrical driver and rectangular expansion region), (ii) the spatial distribution of the magnetic filter field (a complex three-dimension structure), (iii) the inductive coupling to the plasma (via a cylindrical coil), and (iv) the source operation at low gas pressures ($p \geq 0.3$ Pa). Therefore, the following simplifications in the treatment of the problem are involved: (i) reduction of the model dimensions from 3D to 2D, (ii) a Gaussian axial profile of the filter field, (iii) localized external power deposition in the driver region described by a super-Gaussian profile, and (iv) manner of accounting for the inertia term in the momentum equations of the positive ions.

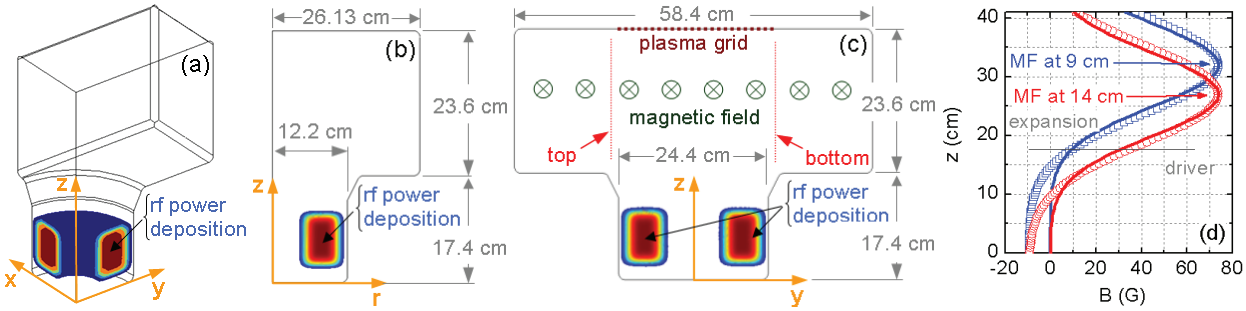

FIGURE 1. Modeling domains used in the simulations for the three cases considered: a quarter of the 3D geometry (a), the 2D axially-symmetric geometry (b) and the 2D geometry with a planar symmetry (c). The size and the RF power deposition region are given. (d) Axial variations of the magnetic field for the two positions of the filter (at 9 cm and 14 cm read from the plasma grid) considered: the calculated values [12] are given by the symbols and the solid curves show their fitting to the Gaussian profiles used in the model.

Figure 1 shows the modeling domains of the three geometries considered here and the manner of the power deposition to the driver. The 3D geometry (Fig. 1(a)) has the exact shape and size of the IPP prototype RF source. However, due to numerical difficulties here, it is considered without a magnetic filter. This 3D model is used as a reference point for choosing a proper geometry (axially-symmetric and planar) for a two-dimensional model description. The symmetry of the source along its axis – in the (x-z)- and (y-z)-planes – has been employed in the 3D model. The 2D geometry with the axial symmetry (Fig. 1(b)) preserves the exact shape and size of the driver, but modifies the rectangular expansion region to a cylinder with a radius preserving its surface. The model within this geometry is without MF since the drifts related to the filter field could not be included in the description of the source operation. The 2D geometry with the planar symmetry (Fig. 1(c)) corresponds to a flat configuration of both the driver and the expansion region that is in a plane perpendicular to the magnetic field (i.e., an axial cross-section of the 3D-case in the (y-z)-plane at $x = 0$). This geometry does not involve the additional losses due to the third dimension, but accounts for the E×B and diamagnetic drifts. Consequently, the model within the 2D geometry with

a planar symmetry is used for showing the influence of the magnetic filter and of the bias potential applied to the plasma grid on the spatial structure of the discharge. This model is also involved in the benchmark of the code to experimental data [12]. The Gaussian axial profile used for the magnetic filter field is with the same maximum value and approximately with the same width as those calculated (Fig. 1(d)). The field is orientated perpendicularly to the modeling domain as it is shown in Fig. 1(c); a constant value of its induction is taken in the *y*-direction. Such a spatial profile of the filter field does not account for the presence of a magnetic field in the driver as well as for its variation in the *y*-direction, but permits to identify clearly the effects of the plasma expansion from the driver into the expansion volume and through the magnetic filter.

The model is within the fluid plasma theory for a hydrogen discharge in a free-fall regime. The charged particles involved in the model are as in [8]: electrons and the three types of positive hydrogen ions. The negative hydrogen ions are not involved in the model since the source is based on a surface production and, therefore, they do not take part in the plasma bulk processes. The positive caesium ions are also not involved, although their distribution depends on the plasma parameters. Due to a high dissociation degree of the hydrogen molecules ($N_a/N_m > 0.2$), both hydrogen atoms and molecules are included in the model. The energy balance of the hydrogen heavy particles (neutrals and positive atoms) is not considered, since it does not influence strongly the spatial structure of the charged particles [13]. The free-fall regime of discharge maintenance is specified by accounting for the inertia term in the momentum equations for the positive ions according to a previously developed procedure [14]. Thus, the initial set of equations includes the continuity equations of the charged particles, respectively, electrons (α = e) and the three types of positive ions ($\alpha \equiv j$ = 1, 2, 3 for H^+, H_2^+ and H_3^+ ions), the continuity equation for the hydrogen atoms, the electron energy balance equation and the Poisson equation:

$$div\,\mathbf{\Gamma}_\alpha = \frac{\delta n_\alpha}{\delta t} \tag{1}$$

$$div(-D_a \nabla N_a) = \frac{\delta N_a}{\delta t} \tag{2}$$

$$div\,\mathbf{J}_e = P_{ext} + P_{coll} - e\mathbf{\Gamma}_e \cdot \mathbf{E}_{dc} \tag{3}$$

$$\Delta\Phi = -\frac{e}{\varepsilon_0}\left(\sum_{j=1}^{3} n_j - n_e\right). \tag{4}$$

The density of the hydrogen molecules is related to that of the atoms through the equation of state $p = \kappa T_g(N_a+N_m)$, where κ is the Boltzmann constant and T_g is the gas temperature; N_a and N_m are, respectively, the densities of the hydrogen atoms and molecules. In (1-4) n_α are the densities of the different types of charged particles and $\mathbf{\Gamma}_\alpha$ are their fluxes, D_a is the diffusion coefficient of the hydrogen atoms, $\mathbf{J}_e$ is the electron energy flux, Φ is the dc electric field potential ($\mathbf{E}_{dc}$ = -grad Φ); e and ε_0 are, respectively, the elementary charge and the vacuum permittivity.

The magnetic fields typically used are such that only the electrons are magnetized. This affects the electron flux and the electron energy flux in the (*y*-*z*)-plane that is perpendicular to the magnetic field. The *y*- and *z*- components of the electron flux $\mathbf{\Gamma}_e$

$$\Gamma_{e(y,z)} = b_{\perp e} n_e \partial_{(y,z)}\Phi - D_{\perp e}\partial_{(y,z)} n_e - D^T_{\perp e}\frac{n_e}{T_e}\partial_{(y,z)} T_e \pm b_{de} n_e \partial_{(z,y)}\Phi \mp D_{de}\partial_{(z,y)} n_e \mp D^T_{de}\frac{n_e}{T_e}\partial_{(z,y)} T_e \tag{5}$$

account for electron mobility, diffusion and thermal diffusion across the magnetic field (the first three terms in the right-hand side of (5)) as well as for the $\mathbf{E}\times\mathbf{B}$ drift and for diamagnetic drifts due to density and temperature gradients as given by the last three terms in (5). Here, $b_{\perp e} = b_{\|e}/(1 + (\Omega_e/\nu_e)^2)$, $D_{\perp e} \equiv D_{\perp e}{}^T = D_{\|e}/(1 + (\Omega_e/\nu_e)^2)$, $b_{de} = (\Omega_e/\nu_e)b_{\perp e}$ and $D_{de} \equiv D_{de}{}^T = (\Omega_e/\nu_e)D_{\perp e}$, where $b_{\|e} = e/m_e\nu_e$ and $D_{\|e} = T_e/m_e\nu_e$ are the mobility and diffusion coefficients along the magnetic field; $\Omega_e = eB/m_e$ is the electron gyro-frequency (with m_e being the electron mass) and ν_e is the frequency of elastic collisions with atoms and molecules.

The *y*- and *z*- components of the electron energy flux $\mathbf{J}_e$

$$J_{e(y,z)} = -\chi_{\perp e}\partial_{(y,z)} T_e \mp \chi_{de}\partial_{(z,y)} T_e + \frac{5}{2} T_e \Gamma_{e(y,z)} \tag{6}$$

involve the thermal flux across the magnetic field and the thermal flux related to the diamagnetic drift, both forming the conductive energy flux, as well as thermal energy and pressure force work carried by the directed velocity, forming the convective energy flux. In (6) $\chi_{\perp e} = \chi_{\|e}/(1 + (\Omega_e/\nu_e)^2)$ and $\chi_{de} = (\Omega_e/\nu_e)\chi_{\perp e}$, where $\chi_{\|e} = (5/2)T_e D_{\|e}$ with T_e being the electron temperature.

The processes having the main contribution to the charged-particle and neutral-specie production and destruction, included in the right-hand sides of (1) and (2), are: ionization and dissociation of molecules, dissociation of H_2^+- and H_3^+-ions, dissociative recombination of H_2^+-ions, heavy particle collisions, ionization of atoms and atom recombination at the walls. The electron energy losses in collisions P_{coll} are via atom excitation and ionization, dissociation, ionization, excitation of vibrational and singlet states of the molecules and elastic collisions of electrons with atoms and molecules. The last term in the right hand side of (3) accounts for the electron energy losses for maintenance of the dc field in the discharge and P_{ext} is the external power deposition.

The boundary conditions for the continuity equations of the charged particles (1) and for the electron energy balance equation (3) are for the fluxes at the walls, as given in [8]. The plasma grid is biased with respect to the metal walls of the source. Therefore, a zero potential of the dc electric field at the walls and a given positive value of the potential at the plasma grid are used as boundary conditions for the Poisson equation (4). The boundary condition for the atoms accounts for their wall recombination, with the value of its efficiency (γ) for a metal wall.

RESULTS AND DISCUSSIONS

Presented here are results for the spatial distribution of the plasma parameters: electron density n_e and temperature T_e, densities of the H^+, H_2^+ and H_3^+ ions as well as plasma potential Φ. They are obtained at an absorbed RF power of 40 kW, gas temperature of $T_g = T_i = 600$ K and a recombination efficiency $\gamma = 0.4$ of the hydrogen atoms at the walls. The latter gives values of $N_a/N_m = (0.2 - 0.6)$ which are in general agreement with those measured. The results given in the first subsection are obtained from the three models – 3D, 2D with an axial symmetry and 2D with a planar symmetry – without a magnetic filter and without a bias potential applied to the plasma grid, at a higher gas pressure (1.6 Pa). The latter is due to numerical difficulties occurring in the 3D code at lower pressure. The results given in the second and third subsections are obtained from the 2D model with a planar symmetry at a low gas pressure (0.6 Pa), with and without a magnetic filter and for different values of the bias potential applied to the plasma grid. The positions of the MF (i.e., the position of the maximum of the magnetic field induction) are 9 cm and 14 cm, read from the plasma grid. The filter field in its maximum is $B = 74$ G (Fig. 1(d)), as in the experiments [12]. The discussions on the influence of the magnetic filter and of the bias applied to the plasma grid on the spatial structure of the discharge are based on the charged-particle and electron-energy fluxes, as given by (5) and (6). The third subsection shows how the model agrees with the experimental data [12] obtained from probe measurements carried out with two probes axially movable in parallel in the second chamber of the source.

Influence of the Modeling Domain Geometry

In order to investigate solely the influence of the geometry of the modeling domain on the spatial distribution of the plasma parameters, the results here are obtained without a magnetic filter and without a bias potential applied to the plasma grid; the gas pressure is 1.6 Pa. The model using the 3D geometry is used as a basis for conclusions on the applicability of the two 2D (axially-symmetric and planar) approaches to the actual source geometry.

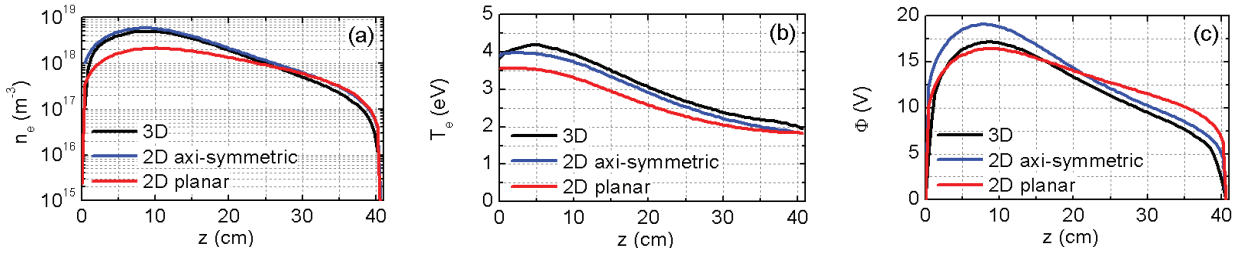

FIGURE 2. On-axis cross-section variations of the electron density (a), of the electron temperature (b) and of the plasma potential (c) obtained within the three model geometries; gas pressure of 1.6 Pa, absorbed power 40 kW, no magnetic filter and no bias potential applied to the plasma grid.

Figure 2 shows that the trends of the axial variations of electron density and temperature as well as of the plasma potential obtained within the 2D axially-symmetric and 2D with a planar symmetry geometries are close to the ones obtained from the 3D model. The deviation is within reasonable limits. The same also refers to the axial variation of the plasma parameters in the off-axis cross-sections in the second chamber (along the path of the "top" probe,

discussed in the third subsection). Therefore, it could be concluded that without a magnetic filter and without a bias potential applied to the plasma grid the two 2D model geometries represent accurately the complex 3D structure of the source.

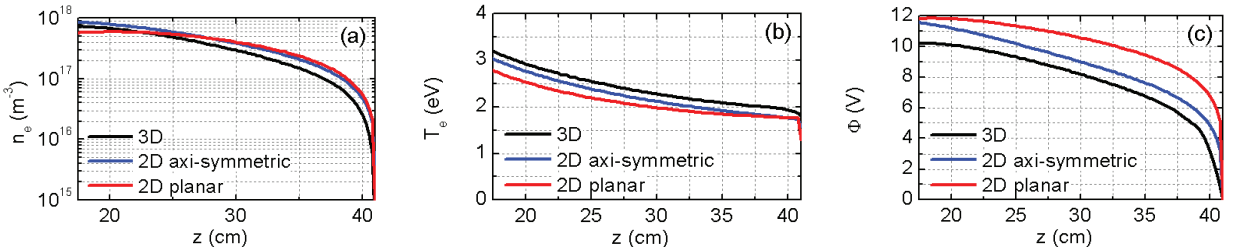

FIGURE 3. Off-axis cross-section variations (at y = -11.2 cm) of the electron density (a), of the electron temperature (b) and of the plasma potential (c) obtained within the three model geometries considered; the same conditions as in Fig. 2.

Influence of the Magnetic Filter and of the Bias Applied to the Plasma Grid

The results in this subsection are obtained from the 2D model with a planar symmetry, which permits accounting for the drifts involved by the magnetic filter. The gas pressure is low (0.6 Pa) and the absorbed power is 40 kW. Due to the low gas pressure and to the localized power deposition, the charged particles and energy fluxes are those controlling the discharge behavior (i.e., the discharge regime is strongly nonlocal [11]). In the figures below these fluxes are shown by normalized arrows (giving only the direction of the given flux). Also contour plots are added for presenting the mutually related variations of the plasma parameters.

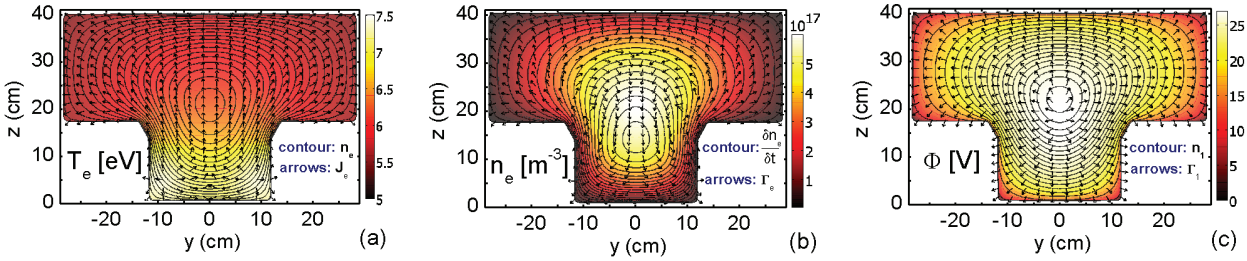

FIGURE 4. Spatial distribution of the electron temperature (a), of the electron density (b) and of the plasma potential (c) obtained without a magnetic filter from the 2D model with a planar symmetry. The absorbed power is 40 kW; p = 0.6 Pa and U_{PG} = 0 V.

In order to identify the effect of the magnetic filter on the spatial distribution of the plasma parameters, the discussion of the results starts with the case without a magnetic field and without a bias potential applied to the plasma grid (Fig. 4). In sources [13] with the configuration of the IPP RF prototype, the effects of nonlocality lead to shifting the maximum of the electron density (Fig. 4(b)) and of the plasma potential (Fig. 4(c)) into the expansion region, while the maximum of the electron temperature (Fig. 4(a)) is in the region of the power deposition in the driver. The maxima of n_e and Φ, as well as the maximum of the electron production and losses via collisions (i.e., the right hand side ($\delta n_e/\delta t$) in (1) shown by the contour lines in Fig. 4(b)) are at different positions. The electron (arrows in Fig. 4(b)) and ion (arrows in Fig. 4(c)) fluxes are also completely different from each other, both in their magnitude and direction. The fluxes of the positive ions, following the dc electric filed, are towards the walls. In contrast, the electron flux is a vortex flux as it has been also observed before, in a model of a small-size two-chamber source [11]. Among the three type of positive ions the atomic ions (contour lines in Fig. 4(c)) are with the highest density. The electron energy flux (arrows in Fig. 4(a)) is mainly a conductive flux, which determines the smooth decrease of T_e from its maximum in the power deposition region towards the walls of the source.

Involving the magnetic filter (without applying a bias potential to the PG) leads to a strong reduction of the electron diffusion and thermal conductivity across the magnetic field which suppresses the nonlocality in the discharge behavior and the plasma is "pushed" back in the driver region, as shown in Fig 5. The plasma existence in the second chamber of the source (where the MF is located) is now due to plasma expansion from the driver. Moreover, because of the different size of the driver and of the second chamber of the source, the effects of plasma

expansion through the filter field (known from a former study [8] of a discharge in an one-chamber source) are influenced by effects of plasma expansion in a bigger-volume second chamber. In the discussions below on the spatial distribution of n_e, T_e and Φ, first the effects of the MF are presented and then the modifications due to plasma expansion in the bigger-volume second chamber are discussed.

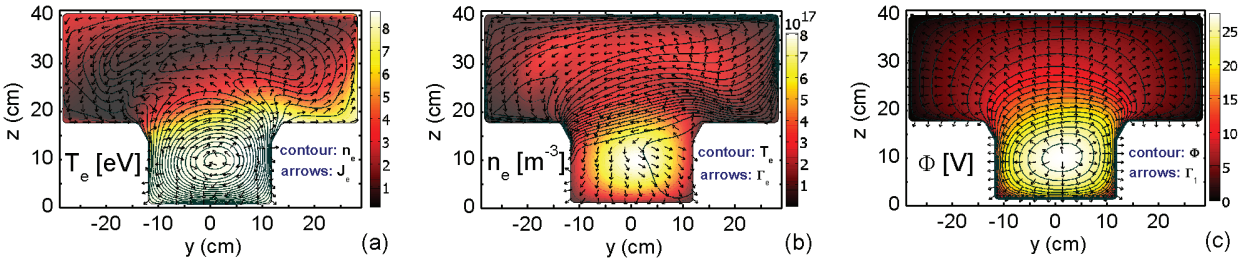

FIGURE 5. The same as in Fig. 4, but with a magnetic filter (74 G) positioned 9 cm away from the plasma grid.

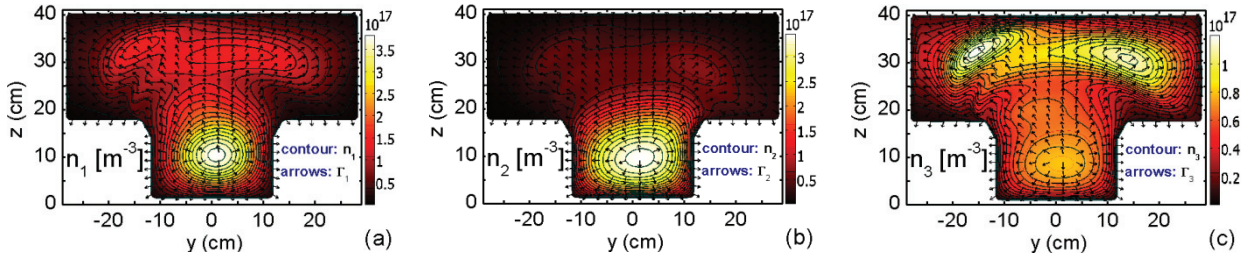

FIGURE 6. Spatial distribution of the densities of H^+ (a), of H_2^+ (b) and of H_3^+ (c) obtained for the conditions in Fig. 5.

As can be seen in Fig. 5(a), a strong axial drop of the electron temperature with a formation of a low T_e-region (with the shape of a groove) in the vicinity of the MF, followed by an increase behind the filter is the major effect of the magnetic filter on T_e. This result is in agreement with Refs. [8-10]. It is caused by the fluxes forming the total electron energy flux (6) – given by arrows in Fig. 5(a) – in the region of the MF. The detailed analysis of $\mathbf{J}_e$ shows that, as in a single chamber source [8], the reduced – by the filter field – thermal conductivity suppresses the thermal flux in the z-direction (given by the $\chi_\perp \partial_z T_e$-term in (6)) causing the strong axial drop of T_e. The latter triggers a thermal flux in the y-direction associated to the diamagnetic drift (the $\chi_{de}\partial_z T_e$-term in (6)) that leads to an increase of T_e towards the right-side wall of the second chamber. This increase of T_e initiates a thermal flux associated again with a diamagnetic drift, but in the z-direction (the $\chi_{de}\partial_y T_e$-term in (6)). The latter carries energy behind the filter, causing a sharp increase of T_e in front of the PG. This leads to the formation of the low T_e-region in the vicinity of the MF. The bending of the shape of the low T_e-region is an effect added here, in the pattern of the spatial distribution of T_e, due to the two-chamber configuration of the source. It results from the convective part of the electron energy flux (the last term in (6)) driven mainly by the E×B drift (the $-b_{de}n_e\partial_y\Phi$-term in (5)).

Within former studies [8] it was shown that in a single chamber source the effect of the MF on the electron density is a formation of a main maximum of n_e and a secondary (slightly pronounced) one in the region of the filter, both shifted from the source axis in the direction of the E×B drift. Such a pattern of the spatial distribution of n_e is also shown in Refs. [9,10], but without the secondary maximum, which could be attributed to differences in the values of the magnetic induction and in the location of the MF. Here (Fig. 5(b)) n_e has two maxima located on both sides of the low T_e-region. The latter is evident in the contour plots of n_e, given over the color map of T_e (Fig. 5(a)), and also in Fig. 5(b) where the contour plots of T_e are presented over the color map of n_e. As in [8], the structuring of the spatial distribution of n_e results from the fluxes forming $\mathbf{\Gamma}_e$ (shown by the arrows in Fig. 5(b)). Diffusion (the second term in (5)) – suppressed by the MF – acting together with thermal diffusion (the third term in (5)) and diamagnetic drift (the last term in (5)), both driven by the axial gradient of T_e on the two sides of the low T_e-region, causes the formation of these two maxima of n_e. Their separation from each other in the y-direction is an effect of the plasma expansion into the larger-size second chamber of the source. The analysis of $\mathbf{\Gamma}_e$ shows that it is caused by a diamagnetic drift (to the right-side wall) and by an E×B-drift (to the left-side wall). In fact, due to the E×B-drift the total electron flux in front of the PG is predominantly parallel to it.

The obtained spatial distribution of the plasma potential (Fig. 5(c)) is in agreement with the results in [9]. As Fig. 5(c) shows the values of Φ in the second chamber are lower than those without MF (Fig. 4(c)), which results from the reduced – by the filter field – charged particle losses at the PG. However, the values of the plasma potential in the driver are almost not changed and, thus, Φ is with a strong drop at the exit of the driver. The latter initiates an E×B drift in the *y*-directed that drives the electrons to the left. On the other hand, the positive ions are not magnetized (as it could be seen from the total flux of the atomic ions indicated by the arrows in Fig. 5(c)), and as a result, the plasma potential is slightly asymmetric at the exit of the driver.

As mentioned before, the positive ions are not magnetized. However, the changes in the discharge structure caused by the MF influence their spatial distribution (Fig. 6). In the driver H^+ and H_2^+ are the ions with the highest density, while H^+ and H_3^+ dominate in the second chamber. The maxima of the densities of H^+ and H_2^+ are in the driver, whereas that of H_3^+ is in the expansion region. Due to the plasma quasineutrality the distribution of the total ion density is similar to that of n_e (Fig. 5(b)).

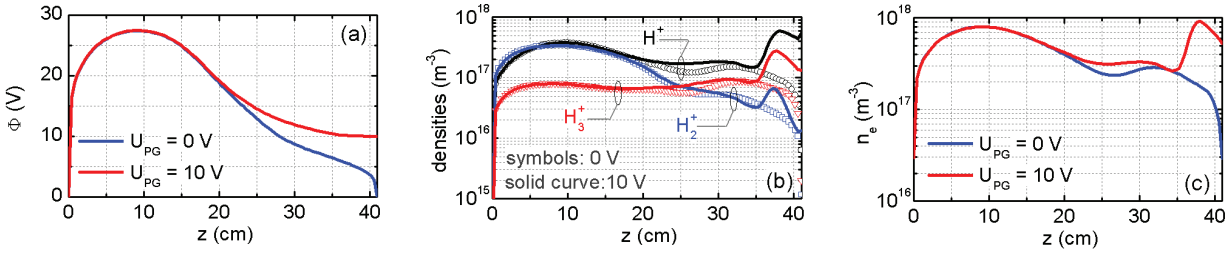

FIGURE 7. Axial cross-sections at $y = 0$ of the plasma potential (a), of the densities of the positive ions (b) and of the electron density (c) obtained at $U_{PG} = 0$ V and 10 V with MF positioned at 9 cm away from PG.

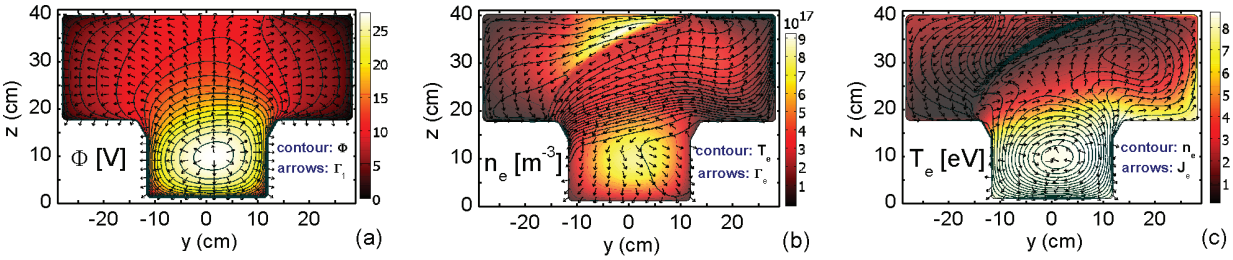

FIGURE 8. The same as in Figure 5, but at applied bias to the plasma grid ($U_{PG} = 10$ V).

Applying a bias potential to the plasma grid affects the plasma parameters, not only locally close to the grid, but also in the entire expansion region (Figs. (7) and (8)). As Figure 7(a) shows, a value of $U_{PG} = 10$ V causes flattening of the axial profile of the plasma potential and a reduction of its axial gradient in front of the PG, which is also evident from the equipotential contours of Φ shown in Fig. 8(a). In fact, higher values of U_{PG} lead to a reversal in the axial profile of the plasma potential in front of the PG. The decreased axial gradient of Φ strongly reduces the E×B drift (which drives the electrons parallel to the PG) and, thus, leads to a shift of the two maxima of n_e towards the right side wall, as it is evident from the contour plots of n_e shown in Figs. 5(a) and 8(c). On the other hand, it reduces also the drift of the positive ions in the dc electric field towards the PG and, strongly dominating over the ionization, leads to an increase of their densities in front of the PG (Fig. 7(b)). The latter stimulates the local accumulation of electrons there (Fig. 7(c)). However, in the vicinity the two sides of the grid the plasma potential drops down towards the surrounding wall (which is at a zero bias potential). As a result, the total flux of the positive ions (shown by arrows for the atomic ions in Fig. 8(a)) in front of the PG is in the transverse direction.

Applying a bias potential to the plasma grid causes also changes in the spatial distribution of the electron temperature and of the shape of the low T_e-region. Figure 8(c) shows that its middle part is closer to the exit of the driver and the top-right one is extended towards the right side wall. The latter correlates with the shift of the maxima of n_e, as it could be seen from the contour plots in Figs. 8(b) and 8(c) The bias potential applied to the PG does not introduce changes in the pattern of $\mathbf{J}_e$ (the arrows shown in Figs. 5(a) and 8(c)). However, it changes the pattern of the total electron flux (the arrows in Figs. 5(b) and 8(b)). The detailed analysis of $\mathbf{\Gamma}_e$ shows that, as in the previous case ($U_{PG} = 0$ V), it is strongly suppressed in the low T_e-region. As a result, the electron flux in the expansion region splits into two parts passing, respectively, on both sides of the low T_e-region (arrows in Fig. 8(b)).

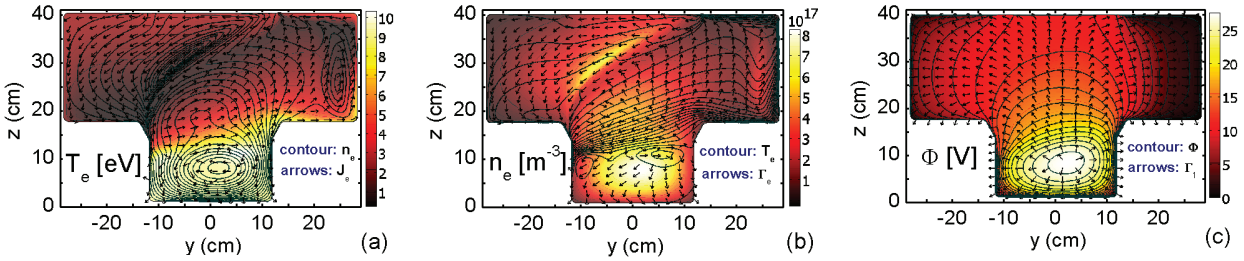

FIGURE 9. Spatial distribution of the electron temperature (a), of the electron density (b) and of the plasma potential (c) obtained from the 2D model with a planar geometry with MF (74 G) positioned 14 cm away from PG and U_{PG} = 10 V; p = 0.6 Pa and absorbed power 40 kW.

Shifting the MF towards the driver (at 14 cm away from the plasma grid), without changing the bias potential of the plasma grid (10 V), shifts the entire profiles of the plasma parameters towards the driver (Fig. 9). However, at this position of the MF, the magnetic field penetrates into the driver region (Fig. 1(d)) and, thus, it influences the plasma parameters not only in the expansion region. Figure 9(a) shows, that now the axial drop of T_e starts in the driver, before the transition between the two chambers. According to the analysis of (6) the thermal flux associated with the diamagnetic drift in the y-direction leads to an increase of T_e: first towards the top-right wall of the driver, and secondly towards the right-side wall of the expansion region. This forms thermal fluxes associated to diamagnetic drifts in the z-direction: starting from the exit of the driver and starting at the right side wall of the second chamber. The former, being the stronger one, leads to further extension of the low T_e-region along the right side wall of the expansion region (Fig. 9(a)). Since, the maxima of n_e are related to the low T_e-region, the right hand side maximum of n_e is further shifted to the right-side wall (Fig. 9(b) and the contour plot in Fig. 9(a)). The total flux of the positive ions (given in Fig. 9(c)) is not affected. However, the electron flux through the low T_e-region towards the right-side wall of the second chamber is kept strongly reduced. As a result, the values of Φ there (Fig. 9(c)) are lower compared with the results for the MF positioned at 9 cm (Fig. 8(a)).

Benchmarking of the Code with Experimental Results

Here, the axial variation of the plasma parameters obtained from the 2D model with a planar symmetry are compared with the values measured by the two Langmuir probes given in Ref. [12]. The probes labeled as "bottom" and "top" are virtually positioned, respectively, at [x = 5 cm, y = ±10 cm] in the 3D geometry (Fig 1(a)). In the two 2D geometries their rotational projections – with respect to the axis of the source – (i.e., the root mean values y = ±11.2 cm) are taken as corresponding positions of the off-axis cross-sections matching the probes path.

Without MF (Fig. 10) the plasma parameters are symmetrical with respect to the source axis and, therefore, the comparison is for one of the probes (the "top" probe). The discharge conditions are: gas pressure p = 0.6 Pa and a bias potential applied to the plasma grid U_{PG} = (9 and 15) V. As it could be seen in Fig. 10, the axial variations of n_e, T_e and Φ obtained from the model are in the trends of those measured, but the manner of their axial decrease is different. Since the axial variation of the plasma parameters given by the 3D- and 2D-models is the same (Fig. 3), this could be addressed to the simplified manner of accounting for the neutral gas-dynamics and the missing energy balance of the heavy particles. Increasing the bias of the plasma grid shifts the entire profile of the plasma potential to higher values. However, the electron density and temperature are not affected.

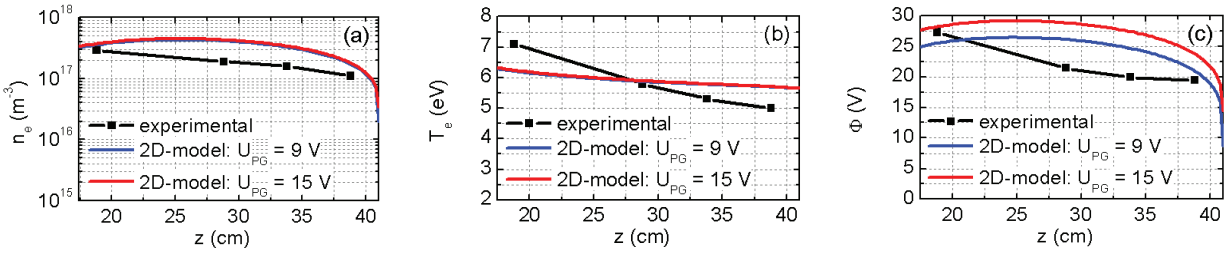

FIGURE 10. Off-axis cross-sections variations of the electron density (a), of the electron temperature (b) and of the plasma potential (c) along the path of the "top" probe obtained from the 2D model with a planar symmetry and from probe measurements carried out without MF; p = 0.6 Pa and absorbed power 40 kW.

The experimental data [12] show that the presence of the MF causes an asymmetry in the axial variations of n_e, T_e and Φ in the expansion region. This is confirmed by the results obtained from the model, as shown in Figs. 11 and 12, respectively, for the two positions of the magnetic filter: 9 cm and 14 cm. The experimental data are obtained at U_{PG} = (18-21) V, whereas, the results from the model are at U_{PG} = 10 V.

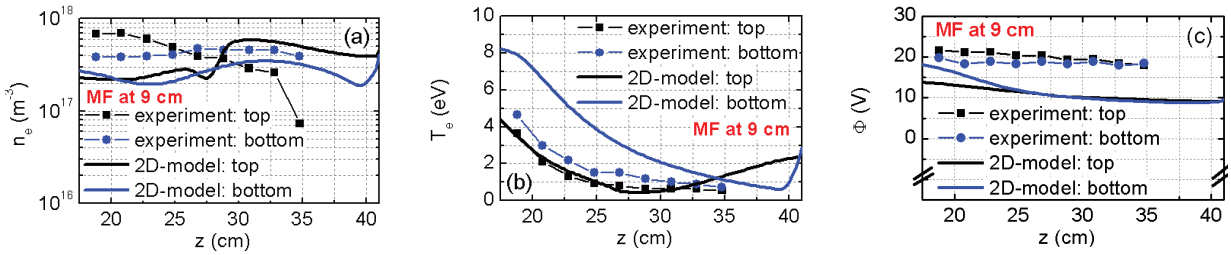

FIGURE 11. Off-axis cross-section variations of n_e (a), of T_e (b) and of Φ (c) along the path of the "bottom" and "top" probes obtained from the 2D model with a planar symmetry and from probe measurements with MF positioned 9 cm away from PG.

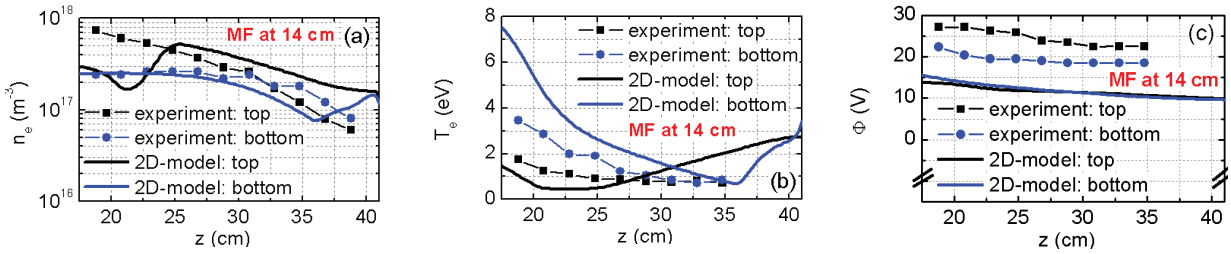

FIGURE 12. The same as in Fig. 11, but for MF positioned 14 cm away from the plasma grid.

Figures 11 and 12 show that the model reproduces the general trend in the axial behavior of the plasma parameters, except for the electron density at the position of the "top" probe. Although n_e is within the range of the measured values, its axial variations does not match well the decrease obtained in the experiments. The agreement between the model and the experiment for the axial profiles of n_e at the position of the "bottom" probe (Figs. 11(a) and 12(a)), however, is good. The electron temperature (Figs. 11(b) and 12(b)) obtained from the model also partially matches the experimental data. The "ripple" in the theoretical profiles of T_e in front of PG is due to the spatial distribution of T_e in the expansion region, with its bended-shaped low T_e-region followed by a sharp increase towards PG (Figs. 8(c) and 9(a)). The axial decrease of the plasma potential obtained from the model in front of PG is almost the same as in the measurements. However, the difference between the theoretical values of Φ at the positions of the "top" and "bottom" probes is not so well pronounced as in the experiments (Figs. 11(c) and 12(c)).

The main conclusion from the benchmarking of the code is that the 2D model with a planar symmetry reproduces the general trend in the axial behavior of the plasma parameters in the source and it could be used for general analysis of the physics governing its operation, both with and without MF. However, there are differences which show that the charged particle and energy fluxes appear with different intensities. Whereas in the model the description of the drifts is restricted to the plane of the modeling domain, in the actual situation the fluxes have a 3D structure due to the 3D distribution of the magnetic field. This requires more detailed accounting for the magnetic field distribution as well as for the neutral gas-dynamics and energy balance of the heavy particles in the model.

CONCLUSIONS

An existing model of the magnetic filter operation [8], based on the fluid plasma theory, has been extended to the configuration and the operational conditions of the IPP prototype RF negative hydrogen ion source. The obtained results for the spatial distribution of the plasma parameters in the source account for the magnetic filter field with its actual field induction and location as well as for the plasma grid with the bias applied to it. The choice of a modeling domain geometry, proper for the description of the source, the influence of the magnetic filter and of the bias applied to the plasma grid on the spatial structure of the discharge, as well as the benchmark of the code with experimental data from probe diagnostics have been stressed on in the study.

It is shown that without a magnetic filter and a bias applied to the plasma grid the two 2D geometries considered, respectively, with an axial-symmetry and with a planar symmetry represent accurately the complex 3D structure of

the source. Since the 2D model with a planar symmetry provides the complete picture of the operation of the magnetic filter (via accounting for the E×B and diamagnetic drifts) it has been used in the two-dimensional model description of the IPP prototype RF negative ion source.

The results obtained without a magnetic filter display a discharge behavior which is controlled by strong nonlocality leading to a shift of the maxima of the electron density and of the plasma potential into the expansion region, while the maximum of the electron temperature is in the power deposition region in the driver. With a magnetic filter, the strong reduction of the transport coefficients caused by the filter field suppresses the nonlocality in the discharge behavior and the plasma is "pushed" back in the driver region. Effects of the plasma expansion into the bigger volume of the second chamber are superimposed on the effects of plasma expansion through the transverse magnetic field. The magnetic filter causes a strong axial drop of the electron temperature in the vicinity of the filter and leads to formation of a region of low electron temperature in its spatial distribution there, accompanied by a formation of maxima of the electron density, also in the filter region. A bended shape of the region of a low electron temperature and strong separation of the two maxima of the electron density in the filter region are the modifications due to the two-chamber source configuration. They are introduced mainly by diamagnetic drifts, caused by temperature gradients, and by E×B-drifts. Applying a bias to the plasma grid in the presence of a magnetic filter affects the spatial distribution of the plasma parameters not only locally, but also in the entire expansion region. It changes the shape of the region of a low electron temperature and shifts the two maxima of the electron density (which appear with different amplitude) in a direction opposite to that of the E×B drift. Shifting the magnetic filter towards the driver shifts the entire pattern towards the driver. In addition, the region of a low electron temperature is further extended along the right side wall of the second chamber, shifting the maximum of the electron density associated with it.

Benchmarking the code with experimental results shows that the model reproduces the general trend in the axial behavior of the plasma parameters in the IPP RF negative ion source and it could be used for general analysis of the physics governing its operation. The differences in the results obtained from the code and the experiments could be attributed to the 3D structure of the charged particle and energy fluxes associated to the actual topology of the magnetic filter.

ACKNOWLEDGMENTS

St. Lishev thanks Prof. Dr. A. Shivarova for discussions. This work has been carried out within the framework of the EUROfusion Consortium and has received funding from the European Union's Horizon 2020 research and innovation programme under grant agreement number 633053. The views and opinions expressed herein do not necessary reflect those of the European Commission.

REFERENCES

1. M. A. Lieberman and A. J. Lichtenberg *Principles of Plasma Discharges and Materials Processing* (New York: Wiley, 2nd edn, 2005).
2. R. S. Hemsworth and T. Inoue, IEEE Trans. Plasma Sci. **33**, 1799–813 (2005).
3. R. Hemsworth et al, Nucl. Fusion **49**, 045006 (2009).
4. E. Speth et al, Nucl. Fusion **46**, S220 (2006).
5. P. Franzen et al, Nucl. Fusion **47**, 264 (2007).
6. U. Fantz et al, Plasma Phys. Control. Fusion **4**9, B563–80 (2007).
7. U. Fantz et al, Nucl. Fusion **49**, 125007 (2009).
8. St. Kolev, St. Lishev, Kh. Tarnev, A. Shivarova and R. Wilhelm, Plasma Phys. Control. Fusion **49**, 1349 (2007).
9. G. J. M. Hagelaar and N. Oudini, Plasma Phys. Control. Fusion **53**, 124032 (2011).
10. G. Fubiani et al, Phys. Plasmas **19**, 43506 (2012).
11. Ts. V. Paunska, A. P. Shivarova, Kh. Ts. Tarnev and Ts. V. Tsankov, AIP Conf. Proc. **1097**, pp. 12-21 (2009).
12. L. Schiesko, P. McNeely, P. Franzen, U. Fantz and the NNBI Team, Plasma Phys. Control. Fusion **54**, 105002 (2012).
13. D. Todorov, Kh. Tarnev, Ts. Paunska, St. Lishev and A Shivarova, Rev. Sci. Instrum **83**, 02B104 (2014).
14. St. Lishev, A. Shivarova and Kh. Tarnev, J. Plasma Phys., **77**, No. 4, pp. 469-478 (2011).